Kinematic analysis of fault-slip data

RANDALL MARRETT and RICHARD W. ALLMENDINGER

Department of Geological Sciences and Institute for the Study of the Continents, Cornell University, Ithaca,
NY 14853-1504, U.S.A.

Abstract—An array of graphical and numerical techniques facilitate qualitative and quantitative kinematic analysis of fault-slip data. Graphical contouring and Bingham statistics of the shortening and extension axes for kinematically scale-invariant faults characterize the distributions and orientations of the principal axes of average incremental strain. Numerical analysis by means of moment tensor summation yields the orientations and magnitudes of the principal strain axes as well as rotational information. Field data can be weighted for moment tensor summation using measurements of fault gouge thickness and/or fault plane width, from which average displacement and fault area can be estimated. The greatest uncertainties of kinematic analysis derive from assumptions about the weighting of the data, the effects of post-faulting rotation on the data, the degree to which sampling is representative of the entire fault population, and the spatial homogeneity of strain. These assumptions can be evaluated for a specific data set. Geometric criteria can distinguish the kinematic heterogeneities produced by triaxial deformation, anisotropy reactivation, strain compatibility constraints and/or multiple deformations. Strain compatibility, material anisotropy and heterogeneity may be characterized by integrating the results of kinematic and dynamic fault-slip analyses.

INTRODUCTION

MANY fundamental tectonic processes can only be studied directly in regions of active tectonics. Evidence of neotectonic deformation is largely limited to brittle deformation in the upper crust, because rocks deforming by crystal-plastic mechanisms are unexposed. Faulting provides the most useful constraints on brittle deformation in modern orogens for several reasons: (1) faults commonly accommodate the largest magnitude of deformation among brittle mechanisms; (2) faults are effectively penetrative at the Earth's surface on a regional scale; (3) seismicity describes some fault activity at depth; and (4) faults commonly can be well dated.

The observations that characterize the kinematics of a fault are the orientation of the fault plane, the orientation of the slip direction, and the sense-of-slip; these data collectively form a fault-slip datum. Fault-slip data can be measured in the field at exposures of faults and can also be gleaned in a somewhat ambiguous form from fault-plane solutions of earthquakes. Additional data are necessary to specify the deformation magnitude of a fault, as discussed in detail below: the average displacement and the fault surface area (for an exposed fault) or the seismic moment (for an earthquake).

The classic work of Anderson (1951) was among the first attempts to relate fault geometry and kinematics to driving stresses. More recently, considerable effort has been directed toward formulating inverse methods of determining stress—here referred to as dynamic methods—from fault-slip data using both numerical techniques (e.g. Carey & Brunier 1974, Etchecopar *et al.* 1981, Armijo *et al.* 1982, Angelier 1984, Gephart & Forsyth 1984, Michael 1984, Reches 1987, Gephart 1988, Huang 1988) and graphical techniques (Arthaud 1969, Angelier & Mechler 1977, Reches 1983, Aleksan-

drowski 1985, Lisle 1987). All dynamic methods assume that faults slip in the direction of shear stress resolved on the fault plane (Wallace 1951, Bott 1959), which requires that stress is homogeneous and that faults do not interact mechanically. Additionally, the dynamic methods assume that sampling is representative and that there has been no post-faulting reorientation of the fault-slip data. These assumptions commonly are not evaluated.

Kinematic analyses of faults are far fewer, perhaps because of the difficulties of applying continuum mechanics to an inherently discontinuous phenomenon. Wojtal (1989) has proposed a two-dimensional graphical approximation for finite strain. Here, we describe a three-dimensional incremental strain analysis via a seismological approach (Kostrov 1974, Molnar 1983) which is more suitable for regional analysis in which the orientations of the principal axes, and their variation with fault magnitude, are of greater interest than the magnitudes of the axes. All quantitative kinematic methods present practical problems for field-based studies because they require weighting the fault-slip data with the displacement and fault surface area. We consider several empirical scaling relationships for faults, including fault gouge thickness and width, that allow estimation of these parameters with field data. A simpler graphical kinematic method can be applied if fault systems can be shown to be scale-invariant.

Several of the assumptions made in kinematic analysis (e.g. rotation, sampling and spatial homogeneity) are analogous to those made in dynamic analyses, however specific tests of each assumption are simple to carry out, as demonstrated here. Techniques for analyzing kinematically heterogeneous sets of fault-slip data produced by triaxial deformation, anisotropy reactivation, strain compatibility constraints and/or multiple deformations

are also presented. Finally, we compare the results of fault-slip analyses of the 1971 San Fernando, California, earthquake sequence using graphical and numerical kinematic methods as well as graphical and numerical dynamic methods, and evaluate the strengths and weaknesses of each method.

THEORETICAL BACKGROUND

The calculation of the incremental strain of a region due to faults within it has already been solved for seismological problems (Kostrov 1974, Molnar 1983). The seismic moment (M_o; see Table 1 for symbols) of earthquakes is simply related to average displacement (u_{ave}) and fault surface area (n) (Aki 1966):

$$M_o = \mu u_{ave} n, \tag{1}$$

where μ is the elastic shear modulus. Closely related is the geometric moment (Sammis et al. 1987), a purely kinematic measure of deformation magnitude which simply omits the shear modulus:

$$M_g = u_{ave} n. \tag{2}$$

If slip on the three-dimensional array of faults is much smaller than the dimensions of the region, the average incremental displacement gradient (∇u) accommodated by each fault can be calculated (Molnar 1983, who referred to this quantity as the "asymmetric moment tensor"). The tensor describing the kinematics of a fault is asymmetric because of the inherent rotation of simple shear deformation, and is calculated by forming the diad product of the unit average displacement vector ($\hat{u}$) and the unit normal vector to the fault plane ($\hat{n}$). ∇u is determined for each fault by multiplying the tensor

describing its kinematics by its scalar M_g and dividing by the volume (V) of region of interest:

$$\nabla u_{ij} = \frac{M_g}{V} (\hat{u}_i \hat{n}_j). \tag{3}$$

Single subscripts in i and j indicate vector quantities and double subscripts in i and j indicate tensor quantities, all in Cartesian co-ordinates using the Einstein summation notation. A convention using the sense-of-slip is necessary to uniquely express $\hat{u}$ and $\hat{n}$. The ∇u for all observed faults are then added, yielding the average incremental displacement gradient due to all of the faults studied (∇u^t):

$$\nabla u_{ij}^t = \sum_{faults} \nabla u_{ij}. \tag{4}$$

Because of the small strain assumption, ∇u^t can be decomposed into symmetric and antisymmetric parts, yielding the incremental strain and rotation tensors, respectively. The eigenvectors of the symmetric part of ∇u^t give the orientations of the principal incremental strain axes and the eigenvalues give their magnitudes.

Jackson & McKenzie (1988) argue that the asymmetry of the above tensor is an artifact of Molnar's (1983) implicit assumption that the co-ordinate system is attached to the fault; thus the region, not the fault, rotates. This assumption cannot be evaluated with fault-slip data alone and therefore they prefer Kostrov's (1974) symmetric tensor. This distinction is not as important as it first appears, because Kostrov's tensor and the *symmetric* part of Molnar's tensor are identical. Thus, the asymmetric tensor potentially contains more information, because its antisymmetric component describes *either* the rotation of the region or the rotation of the faults.

Table 1. Symbols used in text

| Symbol	Parameter
u	local displacement (varies with position on fault surface)
u_{max}	maximum displacement of fault
u_{ave}	displacement averaged over fault surface
$\hat{u}$	unit average displacement vector
n	surface area of fault plane
$\hat{n}$	unit normal vector to fault plane
t	local fault gouge thickness (varies with position on fault surface)
w	maximum fault width
e	fault surface ellipticity
μ	elastic shear modulus
c_1	proportionality constant between u and t
c_2	proportionality constant between u_{max} and w^2/μ^2
c_3	proportionality constant between u_{ave} and u_{max}
M_o	seismic moment
M_g	geometric moment
M_g^1	geometric moment of largest fault in study area
M_g^2	geometric moment of second largest fault in study area
V	volume of study region
∇u	average displacement gradient tensor for a fault
∇u^t	average displacement gradient tensor for all faults studied
N	number of faults having $M_g \geq$ some specified value
A	log N having log $M_g \geq 0$
B	negative slope of log N vs log M_g relation for faults
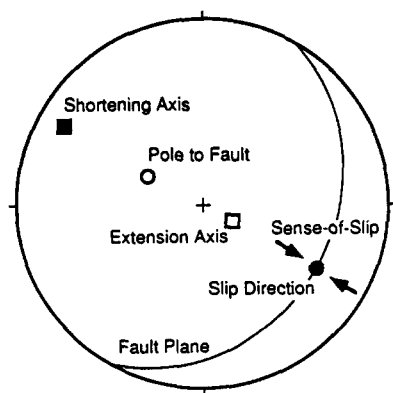
Fig. 1. Geometry of fault-slip kinematics in lower-hemisphere, equal-area stereographic projection. The kinematic axes, slip direction and pole to fault lie in a common plane, with each of the kinematic axes forming angles of 45° with both the slip direction and the pole to fault.

With this background, one can define explicitly the nature of the so-called P- and T-axes familiar to seismologists. The names of the P- and T-axes are unfortunate, because they suggest the stress terms 'pressure' and 'tension'. They are constructed by bisecting the orthogonal nodal planes of a fault plane solution, and thus lie at 45° to those planes. Analytically, however, the P- and T-axes are equivalent to eigenvectors of the symmetric part of the displacement gradient tensor for that fault. Thus, the axes are fundamentally kinematic in nature, representing the principal axes of the incremental strain tensor for the fault. We will refer to them below simply as the shortening and extension axes.

GRAPHICAL AND NUMERICAL KINEMATIC METHODS

Ideally, collection of field data for fault-slip analysis would include: fault plane orientation, slip direction, sense-of-slip, local bedding orientation, average displacement and fault surface area. The fault-slip datum should be measured at a relatively planar part of the fault which is at least subparallel to the megascopic orientation of the fault. Local bedding orientation, used to perform a fold test (see below), should be measured beyond the effects of any drag folding. Numerous features indicative of sense-of-shear have already been described in the literature (e.g. Arthaud & Mattauer 1972, Chester & Logan 1987, Gamond 1987, Means 1987). Because secondary fractures and fault plane surface features commonly are ambiguous indicators of sense-of-shear, as many indicators as possible are desirable. Observations of sense-of-shear should be rated according to relative reliability, in a manner conceptually similar to quality ratings of earthquake locations.

Graphical method

The first step in a kinematic analysis is the graphical construction of the principal incremental shortening and extension axes for a given population of faults. Each pair of axes lies in the 'movement plane' containing the slip

vector and the normal vector to the fault plane, and make angles of 45° with each of the vectors (Fig. 1). The sense-of-slip is necessary to distinguish between the two axes. We emphasize that *no interpretation* is involved in the process of determining the kinematic axes of a fault from field measurements, because essentially one has only converted the measurements into a fault plane solution. Thus, the kinematic axes of a fault are merely an alternative representation of the original data, a representation which is particularly convenient for the various geometric tests described below.

Contouring the shortening and extension axes of an array of faults effectively averages them and provides descriptions of their directional distributions; we use the contouring procedure of Kamb (1959). A potential problem with contouring is that it treats the shortening and extension axes as distinct rather than linked entities, however in our analyses of over 1500 fault-slip data this has not proved important (Marrett *et al.* 1989).

Bingham distribution statistics for axial data provide objective directional maxima of the shortening and extension axes of a fault array (Mardia 1972). The maxima can be calculated separately or in a linked fashion by counting one kind of kinematic axis as positive and the other negative, as has been done for the analyses here. This procedure is identical to moment tensor summation with uniform weighting of the data. Because the results of contouring and Bingham statistical analysis of an array of faults do not account for the magnitudes of deformation, they will be related to the kinematics of the fault array only if the fault kinematics are scale-invariant. This assumption must be tested (see "Weighting test" below) for each data set.

Moment tensor summation and fault-slip magnitude data

Measurements of *average* displacement and fault surface area are needed to determine the magnitude of deformation accommodated by fault movement, yet these quantities usually can be measured only where mining (e.g. Gauthier & Angelier 1985) or seismic data provide three-dimensional control. Several empirical relations make it possible to estimate the magnitude of deformation accommodated by a fault for which u_{ave} and n are uncertain. These estimates are based on field measurements of fault gouge thickness and/or maximum fault width.

For our measurements of cataclastic faults, we defined fault gouge to be material displaced from its initial location with respect to wall rock by more than its longest dimension. As such, this definition deviates from more classical definitions in that it has neither a mineralogical nor a particle size connotation. Recent studies have shown that particles in gouge have a fractal size distribution (e.g. Sammis *et al.* 1987) and thus large lenses of clasts meters in diameter can conceivably represent a coarse fraction of fault gouge.

Measurement of fault gouge thickness (t) in the field presents several problems. Given the presence of asperities, t clearly varies from some maximum amount down

to zero as a function of position along a fault. However, consistent estimates can be made by choosing a tabular part of each fault zone for measurement of gouge thickness. The possible presence of unidentified horses presents another problem, particularly for large faults in incompletely exposed regions. Drag folding and attendant bedding-parallel slip pose an additional problem for large faults, because they can obscure the boundaries of the gouge zone by deforming adjacent wall rock.

Models of fault growth (Sammis *et al.* 1987, Cox & Scholz 1988, Power *et al.* 1988) predict a linear increase of local fault gouge thickness with local displacement (u). Data from cataclastic faults with u ranging from 10^{-2} to 10^4 m fit these models to within an order of magnitude (Scholz 1987, Hull 1988, this paper):

$$u = c_1 t, \tag{5}$$

where c_1 is an empirical constant. We determined an average value of $c_1 = 70$ for Tertiary red beds of northwestern Argentina in an environment of horizontal shortening (Fig. 2); we will use this value below. Hull (1988) independently determined a value of 63 for a wide variety of rock types including Mesozoic sandstones deformed in horizontal extension.

Elliott (1976) suggested that, empirically, the surface trace length of a fault in plan view is linearly proportional to maximum displacement (u_{max}). Walsh & Watterson (1988) argue that maximum displacement is proportional to the square of maximum fault plane width (w), defined as the maximum dimension of a fault plane normal to its slip direction. They show that Elliott's data and newly collected data are empirically consistent, at least for fault widths under 100 km, with the following relationship:

$$u_{max} = \frac{c_2}{\mu^2} w^2, \tag{6}$$

where c_2 is a variable related to the stress drop of earthquakes averaging 2×10^{-4} GPa^2 m^{-1} for faults in a variety of rock types with displacements ranging from 10^0 to 10^5 m.
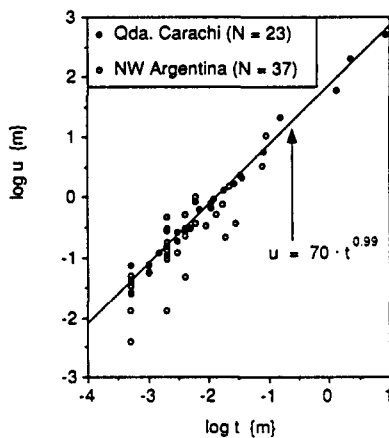
Fault surface trace length usually is measured from air photographs or maps rather than measured directly in the field. Because the complicated regions near fault tip lines are commonly small compared with the length of the fault, the uncertainty in trace length is not severe. More difficult is the assessment of the fault geometry at depth and in the rock now eroded away, which is necessary to relate fault surface trace length (which is generally a chord in a simple elliptical fault model) to w. For many faults there is no alternative to assuming that they are the same, which if incorrect will always lead to an underestimation of w and therefore of u_{max}.

To use one of the empirical relationships above in estimating the deformation magnitude of a fault (preferably using locally determined constants), one must first relate u_{ave} with u and/or u_{max}, and also somehow evaluate n. The fractal nature of faulting (e.g. King 1983, Scholz & Aviles 1986, Turcotte 1986) suggests that the displacement functions of faults (u as a function of position on a fault surface) might be scale-invariant. Detailed studies show that this is generally true (Muraoka & Kamata 1983, Higgs & Williams 1987, Walsh & Watterson 1987), although no data have been evaluated from faults with kilometers of displacement. This implies a simple linear relationship between u_{max} and u_{ave}:

$$u_{ave} = c_3 u_{max}, \tag{7}$$

where c_3 is a constant which depends on the shape of the displacement function. For example, $c_3 = 2/3$ for an elliptical displacement function and $c_3 = 1/3$ for a triangular displacement function (Fig. 3). Faults tend to have displacement functions intermediate between elliptical and triangular (Muraoka & Kamata 1983,
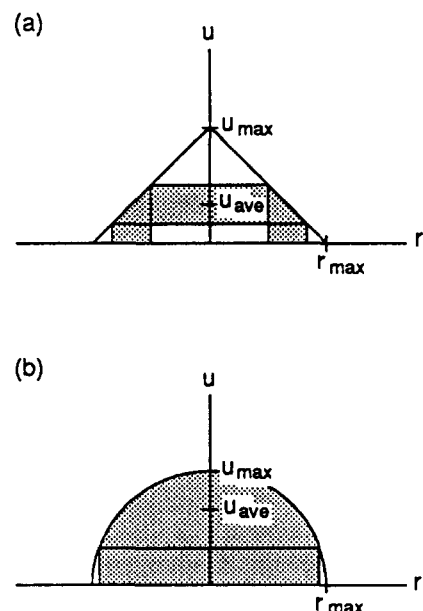
Fig. 2. Log–log plot of fault gouge thickness (t) against displacement (u) for brittle fault zones in northwestern Argentine Andes. The line is a linear regression to the data from Quebrada Carachi: $u = 70 t^{0.99}$; $R^2 = 0.99$.

Fig. 3. (a) Triangular and (b) elliptical displacement functions, showing distance from the center of an elliptical fault (r) against displacement (u). r_{max} occurs at fault tip. Shaded regions indicate where u is within $u_{ave} \pm \frac{1}{2} u_{ave}$. For triangular displacement function $u_{ave} = \frac{1}{3} u_{max}$, and 44% of fault surface falls in shaded region. For elliptical displacement function $u_{ave} = \frac{2}{3} u_{max}$, and 89% of fault surface falls in shaded region.

Higgs & Williams 1987, Walsh & Watterson 1987), so we will use $c_3 = 1/2$ below.

Characterizing the relationship between u and u_{ave} is less trivial. If one were to measure u at many points on a fault in a random way and average them, the result would be a good approximation of u_{ave}. In fact, if one were to measure u at only one randomly chosen point on a fault with an elliptical displacement function, the probability is 89% that u is within 50% of u_{ave} (Fig. 3). When the error is greater than 50%, u_{ave} is always underestimated. Because the displacements observed for faults in typical arrays vary by several orders of magnitude, errors associated with assuming that u is statistically the same as u_{ave} should be relatively small. Thus, we assume:

$$u_{ave} \approx u. \tag{8}$$

Kanamori & Anderson (1975) successfully explained several empirically determined scaling laws of earthquakes using a model in which the surface area of slip is proportional to the square of average slip. Earthquakes and faults are not identical phenomena, because a large fault is the product of many earthquakes which have occurred in approximately the same place. The results of Walsh & Watterson (1988) imply that n is linearly proportional to u_{ave}, as seen by expressing n in terms of w and substituting equations (6) and (7):

$$n = \frac{\pi w^2}{4e} = \frac{\pi \mu^2}{4ec_2c_3} u_{ave}, \tag{9}$$

where e is the ellipticity of the fault surface. Although few data sets are available, data from both normal and thrust faults suggest that e varies between 2 and 3 (Walsh & Watterson 1987); we will use $e = 2$ below.

Substituting equations (5)–(9) into equation (2) yields M_g in terms of t and w:

$$M_g = \frac{\pi \mu^2 c_1^2}{4ec_2c_3} t^2 \tag{10}$$

$$M_g = \frac{\pi c_2 c_3}{4e\mu^2} w^4. \tag{11}$$

These relationships are sufficient for *relative* weighting of the geometric moments among observed faults, however they are insufficient for determining the absolute deformation magnitude for each fault. Using the values of c_1, c_2, c_3 and e cited above and $\mu = 12$ GPa (Walsh & Watterson 1988), approximate relationships for a hard sandstone are:

$$M_g \approx (3 \times 10^9 \text{m}) t^2 \tag{12}$$

$$M_g \approx (3 \times 10^{-7} \text{ m}^{-1}) w^4. \tag{13}$$

We emphasize that these relationships are not as precise as they might appear due to the cumulative uncertainties of the empirical constants, which can be as large as an order of magnitude. They are primarily intended for making order of magnitude estimates of geometric moment where the parameters of faults in a typical array span many orders of magnitude. Subtler

use of estimates from the scaling relationships is unjustified.

APPLICATION OF KINEMATIC METHODS AND TESTS OF ASSUMPTIONS

The accuracy of analytical results from kinematic fault-slip analysis is subject to uncertainties which probably depend less on the accuracy of field measurements than they do on the validity of assumptions: the weighting of fault-slip data, possible reorientation of the fault-slip data, the degree to which sampling is representative of the entire fault population, and, in a limited sense, the spatial homogeneity of strain. We compare the methods and illustrate some tests of assumptions with a data set collected in a trial study area, known as Quebrada Carachi (Fig. 4) in the Andes of northwestern Argentina (Marrett 1990). Fifty-nine measurements were made of 46 faults (large faults were measured in several different places). Local displacement was measured for 23 of the faults and local fault gouge thickness was measured for all faults studied. The results of moment tensor summation for the data set from the study area, as well as for subgroups of the data defined by ranges of u, are shown in Table 2. The graphical method shows simple point maxima of shortening and extension (Figs. 5a & b) which are similar to the results of moment tensor summation (Table 2).

Weighting test

Weighting of fault-slip data is done in moment tensor summation with the geometric moment. Although the graphical kinematic method assumes that fault kinematics are scale-invariant, weighting can be qualitatively assessed by separating a data set into subgroups of faults of different sizes and comparing their kinematics.

The data from the study area, with displacements spanning five orders of magnitude, were separated into five subgroups and the kinematics of each subgroup was analyzed using both Bingham distribution statistics and moment tensor summation (Figs. 5c & d and Table 2). The results of both methods show tight clustering of shortening axes and less tight clustering of extension axes; furthermore, the results of graphical analysis are consistent with the results of moment tensor summation. Fault kinematics appear to be scale-invariant *for these data*, as well as for most other data sets that we and others have collected. If faults generally have scale-invariant kinematics, this represents another fractal characteristic of the faulting process (e.g. King 1983, Scholz & Aviles 1986, Turcotte 1986, Power *et al.* 1987, Sammis *et al.* 1987, Barton *et al.* 1988).

Fold test

Post-faulting reorientation of a fault-slip datum changes the orientations determined for the kinematic axes. The significance of differential rotation about
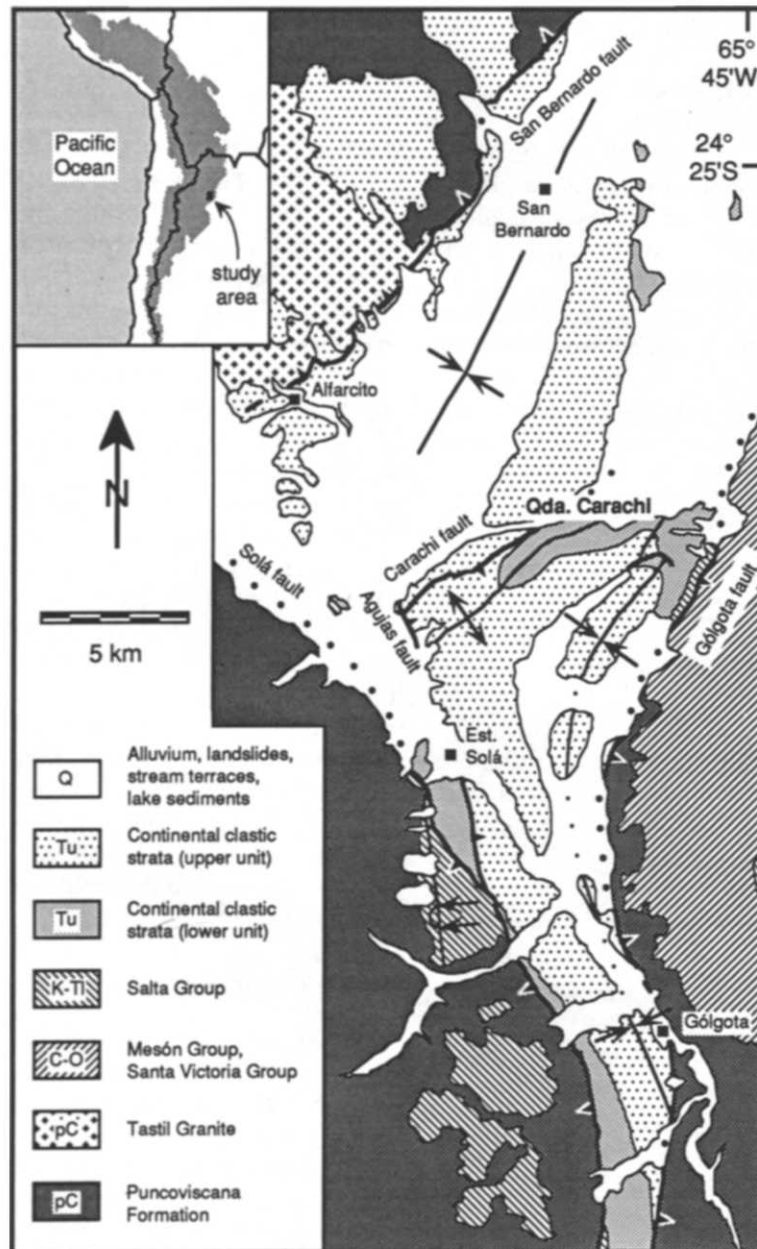
Fig. 4. Geology of Quebrada del Toro, northwestern Argentina (modified from Marrett 1990). Inset shows political borders in solid lines and areas above 3 km average elevation in dark shading.

horizontal axes can be characterized for a given data set by using a fold test similar to those used in paleomagnetic studies. In the fold test, the kinematic axes are rotated by the amount necessary to return local bedding to horizontal. Unfolding only the fault planes or only the slip directions can be inconclusive because many data sets with highly variable fault and/or slip orientations have coherent kinematics. If the unfolding produces kinematics which are more coherent than the kinematics of the faults in present geographic orientation, then

Table 2. Comparison of results from moment tensor summation (weighted by fault gouge thickness) and linked Bingham distribution statistical analysis of fault-slip data from Quebrada Carachi. Directions given in trend and plunge

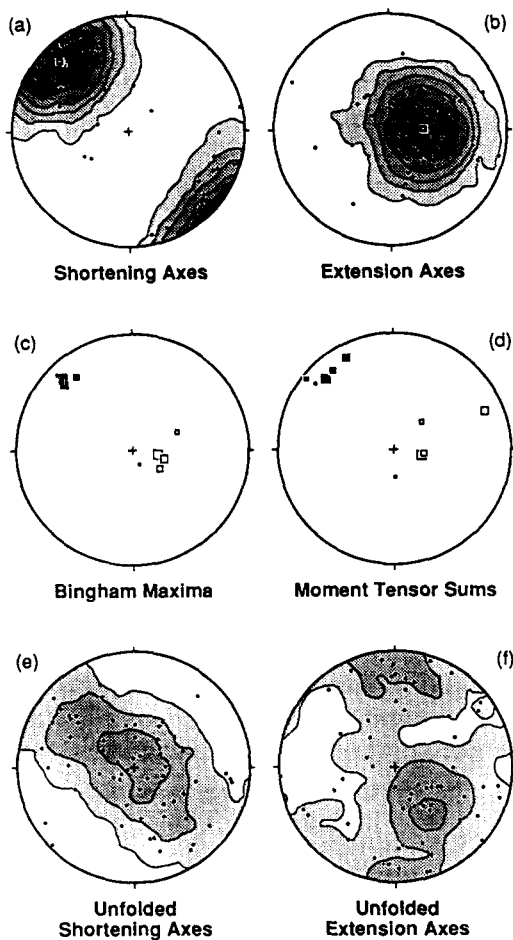| Displacement range (m)	No. of measurements	No. of faults	Moment tensor summation		Linked Bingham distibution maxima	
			Shortening	Extension	Shortening	Extension
all faults	59	46	316°, 17°	102°, 70°	316°, 17°	89°, 67°
100–1000	8	2	316°, 17°	103°, 70°	316°, 15°	100°, 72°
10–100	10	5	333°, 13°	67°, 17°	314°, 20°	106°, 67°
1–10	10	8	322°, 16°	99°, 69°	323°, 22°	125°, 67°
0.1–1	23	23	309°, 04°	46°, 63°	314°, 16°	68°, 56°
0.01–0.1	8	8	310°, 13°	178°, 70°	315°, 10°	156°, 79°

Fig. 5. (a) & (b) Fault-slip kinematics of data from Quebrada Carachi, northwestern Argentina (59 measurements of 46 faults). Solid dots represent kinematic axes, open boxes represent Bingham distribution maxima, and shades represent distributions of 2σ contour intervals (e.g. white areas indicate fewer axes at counting grid points than that found in a uniform distribution minus 1σ; adjacent low density grey areas indicate grid points having numbers of axes within $\pm 1\sigma$ of that in a uniform distribution; adjacent slightly higher density grey areas indicate grid points having numbers of axes with 1–3σ more than that in a uniform distribution; all contour diagrams conform). (c) & (d) Weighting test of fault-slip data from Quebrada Carachi. Largest to smallest boxes represent analyses of fault-slip data subgroups with displacements of 100–1000, 10–100, 1–10, 0.1–1 and 0.01–0.1 m, respectively. Solid boxes represent shortening directions and open boxes represent extension directions. (e) & (f) Fold test of fault-slip data from Quebrada Carachi. Contour diagrams of kinematic axes which have been independently rotated by the amount necessary to return local bedding to horizontal.

folding probably post-dates faulting; otherwise folding probably pre-dates faulting. Regional tilting, domino-style block rotation, and vertical axis rotation cannot be detected with this technique, but can be addressed using regional geologic and paleomagnetic data.

Several NE-verging closed folds cross the study area (Fig. 4). Contour diagrams of the kinematic axes from the study area are much less coherent in the unfolded configuration (Figs. 5e & f) than in the folded configuration (Figs. 5a & b), suggesting that most faulting postdates folding. Approximately horizontal bedding characterizes large areas in and around the study area and suggests that regional tilting has not been important. Major thrust faults flanking the study area dip both NW and SE and suggest that domino-style block rotation did

not occur. Paleomagnetic data have not been collected in this area, so the importance of vertical axis rotation is uncertain.

Sampling test

Due to practical limitations inherent to field-based studies, only a small portion of the faults that exist in a given area are typically sampled. For the same reasons, it is difficult to determine whether the observed faults are representative of the entire fault population. Because many characteristics of faults and earthquakes are fractal, we conjecture that faults follow a power-law number–geometric moment relation, analogous to the frequency–magnitude relation for earthquakes:

$$\log N = A - B \log M_g, \tag{14}$$

where N is the number of faults having geometric moments greater than or equal to M_g, B is analogous to the b-value of earthquakes (because faults and earthquakes are different phenomena, it is unnecessary that the two be identical) and A is a measure of the total number of faults. One may determine A and B for a specific area from the geometric moments of the largest two faults (M_g^1 and M_g^2), however the use of just two faults cannot test the assumption of a power-law number–geometric moment relation. Alternatively, B might be determined by analyzing outcrops at which all faults (above a certain size threshold) can be identified and measured. Preferably, the size range of such outcrops would be as great as possible and the largest faults in the study area would also be analyzed to constrain A. This would allow one to evaluate how well the fault population actually follows a power-law number–geometric moment relation. Using A and B, one can predict the number of faults that exist at any specific size range and quantify the percent of those faults actually observed.

Another measure of sampling is the portion of the total geometric moment sampled. The total geometric moment due to all faults can be written as a function of B and M_g^1 by assuming that the fault array is truly self-similar:

$$\sum_{\text{faults}} M_g = M_g^1 \left[1 + \frac{1}{2^{1/B}} + \frac{1}{3^{1/B}} + \frac{1}{4^{1/B}} + \cdots \right]. \tag{15}$$

Equation (15) converges only for $B < 1$; this is reasonable because $B = 1$ corresponds to the situation in which the sum of geometric moments of faults in each order of magnitude range are about the same. For example, faults with displacements of 1–10 mm would, by virtue of their tremendous numbers, have as much total geometric moment as faults with displacements of 1–10 km. Were $B = 1$ for faults, construction of balanced cross-sections based only on the largest faults would be a useless exercise.

Due to the excellent exposure in the study area, we believe that the two biggest faults were identified (Fig. 6). Based on this assumption, $B = 0.38$. The distance on the number–geometric moment plot between the model
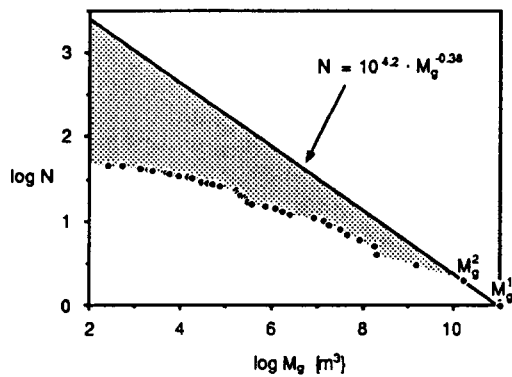
Fig. 6. Sampling test of fault-slip data from Quebrada Carachi (46 faults measured). Log–log plot of geometric moment (M_g) against the number of faults (N) having a geometric moment greater than observed values of M_g. The line represents a model assuming that the two largest faults observed are in fact the largest two faults in the study area and that the entire fault population fits power-law number–geometric moment relationship. Height of shaded area represents degree of undersampling.
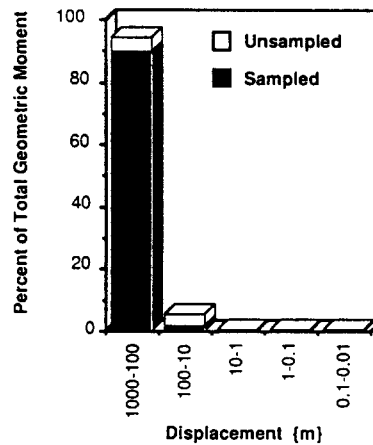

Fig. 7. Bar graph of percent of total geometric moment sampled for faults with displacements of different orders of magnitude at Quebrada Carachi, assuming that the two largest faults observed are in fact the largest two faults in the study area and that the entire fault population fits a power-law number–geometric moment relationship.

line and the points representing the observed faults is a measure of the faults that should exist but which were not measured. For example, there should be 13 faults having $M_g > 10^8$ m³ but only five were measured in the field, so about 38% of those faults were sampled.

For $B = 0.38$,

$$\sum_{faults} M_g \cong 1.3 M_g^1. \tag{16}$$

The largest fault zone alone accounts for nearly 80% of the total geometric moment. This suggests that the prospects of constructing a useful balanced cross-section of the study area are good. The faults measured in the field represent 93% of the total geometric moment (Fig. 7), indicating that sampling is indeed representative of the entire fault population for this data set. However, these estimates are based on the untested assumption that the faults follow a power-law number–geometric moment relation.

Spatial homogeneity test

In principle, the kinematic methods do not assume that fault-slip kinematics are spatially homogeneous. However, group analysis of spatially heterogeneous data can obscure meaningful variation in the data by averaging statistically distinct subgroups. Testing for spatial homogeneity assures that such variation is recognized. The degree of spatial homogeneity can be evaluated for a given data set by analyzing subgroups of faults from different domains and comparing their kinematics.

Comparing the fault kinematics at the different measurement sites in the study area indicates that kinematics are spatially homogeneous; for the purpose of illustration, the data were separated into two subsets representing fault measurements from the NE and the SW parts of the study area (Fig. 8). The kinematics of the two subsets are statistically indistinguishable. Commonly, fault kinematics are statistically homogeneous over large areas. For example, more than 1500 fault

measurements from a region of northwestern Argentina about 400 km long and 200 km wide show remarkably little variation during the Tertiary and a more complex but coherent pattern during the Quaternary (Marrett et al. 1989).

INTERPRETATION OF KINEMATIC HETEROGENEITY

Kinematically heterogeneous faulting, represented by girdle or multi-modal patterns of shortening and/or extension axes, can be produced by several mechanisms:
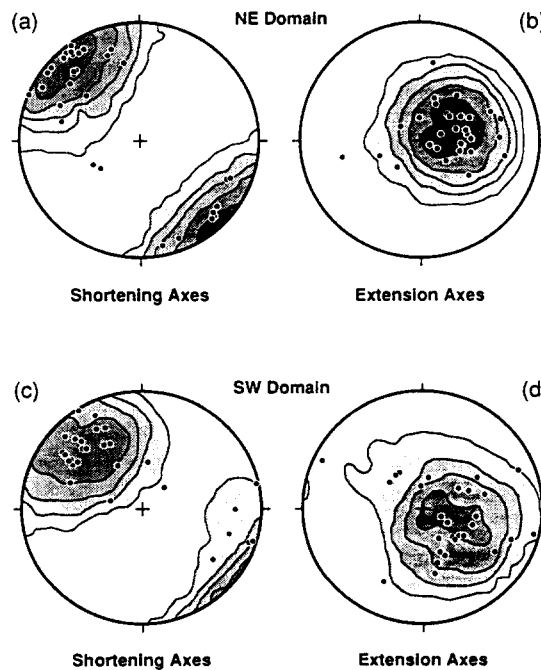

Fig. 8. Spatial homogeneity test of fault-slip data from Quebrada Carachi. Contour diagrams of (a) shortening axes and (b) extension axes of faults in NE part of study area ($N = 36$). Contour diagrams of (c) shortening axes and (d) extension axes of faults in SW part of study area ($N = 23$).

triaxial deformation, anisotropy reactivation, strain compatibility constraints and/or multiple deformations. Geologic evidence independent of fault-slip data provides the clearest indications of these mechanisms, although the absence of such evidence for a specific mechanism does *not* demonstrate its inactivity. Graphical analysis of fault-slip data may allow more complete interpretation of kinematically complex faulting because each mechanism produces distinct patterns of poles-to-faults and slip directions (Fig. 9) which may be used to qualitatively assess the importance of each mechanism in a specific case.

The data previously discussed were kinematically homogeneous (Figs. 5a & b). However, data from a larger area in NW Argentina (Fig. 4) are kinematically heterogeneous because there is a bimodal pattern of shortening axes (Figs. 10a & b). This area, known as Quebrada del Toro (Marrett 1990), includes the study area previously discussed.

Triaxial deformation

Reches (1983) showed that triaxial deformation produces three or four sets of faults arranged with orthorhombic symmetry and an equal number of distinct slip directions, also having orthorhombic symmetry (Fig. 9a). Such patterns have been observed in the field and in experiments (Donath 1962, Aydin & Reches 1982, Reches & Dieterich 1983, Krantz 1988). The degree to which the model of Reches (1983) fits a given data set provides an indication of how important triaxial deformation was in the development of heterogeneous kinematics. The presence of mutually cross-cutting fault sets supports the interpretation of triaxial deformation.

The study area is dominated by four sets of major faults, although they are defined rather indistinctly by maxima in the contour diagram of poles to faults (Fig. 10c). Four distinct maxima of slip directions are ob-

served in the contour diagram of the data. (Fig. 10d). Poles to faults and slip directions commonly scatter much more than the kinematic axes determined from them. The fault sets and slip directions have relatively poor orthorhombic symmetry (Fig. 10e) which is much closer to that of two conjugate pairs, one with dip-slip faults striking NW–SE and the other with dip-slip faults striking NE–SW. Thus, triaxial deformation apparently does not explain the kinematic heterogeneity in this data set.

Anisotropy reactivation

Simple regional deformations can reactivate local, pre-existing anisotropies that are not ideally oriented for accommodating the overall deformation, thus producing locally heterogeneous triaxial deformation. Anisotropies which exist only in units beneath those of interest can nevertheless control the kinematics in the overlying, previously unfractured rock. Because the orientation of a pre-existing anisotropy is arbitrary with respect to the reactivating deformation, slip on the plane of anisotropy

Fig. 10. (a) & (b) Fault-slip kinematics of data from Quebrada del Toro, northwestern Argentina ($N = 222$). (c) Poles to faults and (d) slip directions for data from Quebrada del Toro. Note the greater coherence of kinematic axes than of poles to faults or slip directions. (e) Analyses of triaxial deformation and strain compatibility for fault-slip data from Quebrada del Toro. Maxima of poles to faults in open dots, fault sets in great circles (different conjugate sets represented by different width lines), and maxima of slip directions in solid dots. (f) Analysis of anisotropy reactivation for fault-slip data from Quebrada del Toro. Contour diagram of poles to bedding ($N = 248$) of greenschist basement underlying faulted Tertiary strata at Quebrada del Toro (Omarini 1983).
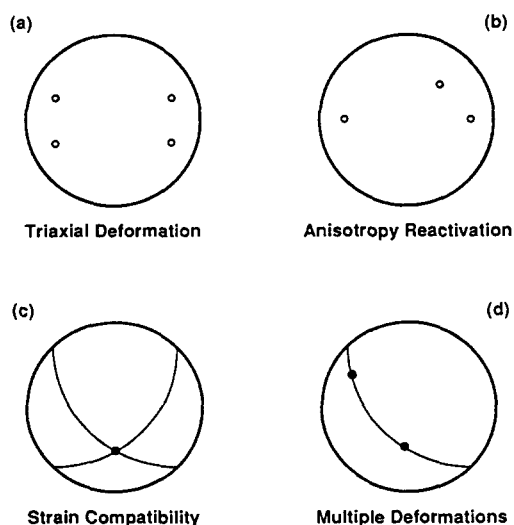

Fig. 9. Models of mechanisms that can produce kinematic heterogeneity. Great circles represent sets of fault planes, open dots represent poles to fault sets, and solid dots represent dominant slip directions of fault sets.
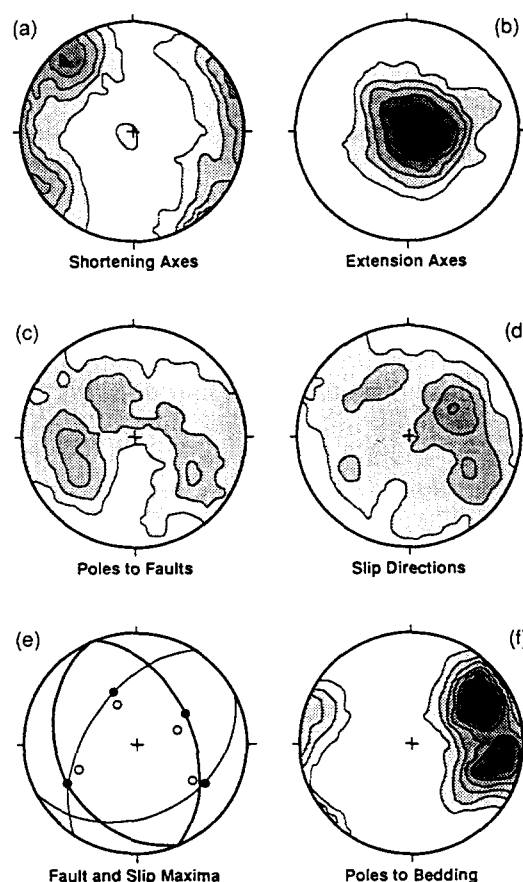
may be unsystematically oblique compared with slip on newly forming faults. Thus, reactivation of a basement anisotropy should produce a fault set and slip directions which are not related to the other fault sets by a conjugate or orthorhombic symmetry (Fig. 9b). Anisotropy reactivation may produce a positive correlation between the orientations of a fault set and basement anisotropy or between spatial changes in fault-slip kinematics and changes in basement anisotropy orientations.

In the study area, a sequence of complexly folded, greenschist facies flysch, in which bedding planes define the most important anisotropies (Fig. 10f), lies unconformably beneath the faulted strata (Omarini 1983). Comparison of basement bedding poles with poles to faults (Fig. 10c) shows that the E-plunging poles to faults match basement anisotropy somewhat, but the west-plunging poles to faults are unrelated to basement anisotropy. The two fault sets with poles plunging to the west are not conjugates because their slip directions are not appropriately oriented (Fig. 10e). Therefore anisotropy reactivation alone cannot produce the observed kinematic heterogeneity.

Strain compatibility

Strain compatibility between two differently oriented faults or fault segments requires that they both must slip parallel to their line of intersection if no additional structures form. A larger difference in the orientations of the faults or fault segments produces a larger difference in their kinematics. This constraint will result in multiple sets of faults which have similar slip directions (Fig. 9c).

Two slip direction maxima for the data from the study area correspond well with intersections of fault sets (Fig. 10e). A detailed comparison of slip directions for the faults which most tightly define the NW- and SW-dipping fault sets (Fig. 11) shows that the SW-dipping faults have mostly coherent slip which is subparallel to the intersection of the fault sets. The NW-dipping faults have quite variable slip, some subparallel with the fault set intersection but most faults have more nearly dip-slip movement. Strain compatibility may have controlled some of the slip on these fault sets, but it cannot

completely explain their slip directions and hence cannot completely explain their kinematic heterogeneity.

Multiple deformations

Multiple deformations commonly produce heterogeneous fault-slip kinematics. A special kind of anisotropy reactivation can result when pre-existing faults are reactivated, generating a second set of striae. Thus, individual faults may show evidence for slip in two or more different directions and a single set of faults may have widely varying slip directions (Fig. 9d). The fault-slip kinematics of one deformation might also be incompatible with the kinematics of another deformation. Independent evidence for multiple deformations include systematic cross-cutting relations between fault sets and mutually exclusive chronologic constraints on fault sets.

The slip directions for NW-dipping faults in the study area have highly variable slip directions, while the slip directions for SW-dipping faults are mostly coherent (Fig. 11). This indicates that the NW-dipping faults have been reactivated whereas the SW-dipping faults have not been. Some of the larger NW-dipping faults have multiple sets of fault striae indicating both dip- and strike-slip movement, confirming the inference based on kinematic analysis. Furthermore, it appears that some of the NW-dipping faults were reactivated *during* the movement of the SW-dipping faults and thus suggests that the former are older than the latter. Strain compatibility may have controlled the slip directions of both fault sets during the later phase of deformation.

Geometric analysis of the fault orientations and slip directions for faults in the study area suggest that multiple deformations are mostly responsible for producing the kinematic heterogeneity observed there. This result is consistent with field relations: the younger NW- and SE-striking faults consistently cut the older NE- and SW-striking faults wherever both are present (e.g. Fig. 4). Based on this criterion, the data can be separated objectively into two kinematically homogeneous subgroups representing the two phases of deformation (Fig. 12).

COMPARISON OF DYNAMIC AND KINEMATIC METHODS

The 1971 San Fernando, California, earthquake sequence is well-studied because of its proximity to a major metropolitan area. Several attempts have been made to understand the dynamics and kinematics of the faulting based on fault plane solution and seismic moment data (e.g. Whitcomb *et al.* 1973, Hadley & Kanamori 1978, Langston 1978, Gephart & Forsyth 1984, Julien & Cornet 1987). The same data are analyzed here using the graphical kinematic method, moment tensor summation and the P–T dihedra stress inversion (Angelier & Mechler 1977) to complement published analytical results from grid search stress inversion (Gephart &
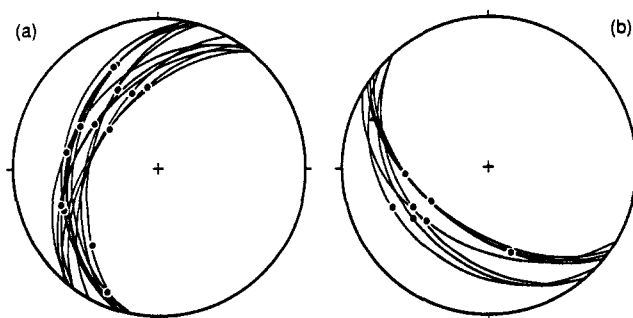

Fig. 11. Analysis of multiple deformations for fault-slip data from Quebrada del Toro. Individual faults and slip directions represented by great circles and solid dots, respectively. (a) Faults striking 190–220° and dipping 30–55° ($N = 13$). (b) Faults striking 120–150° and dipping 30–55° ($N = 7$).

Younger Shortening Axes   Younger Extension Axes

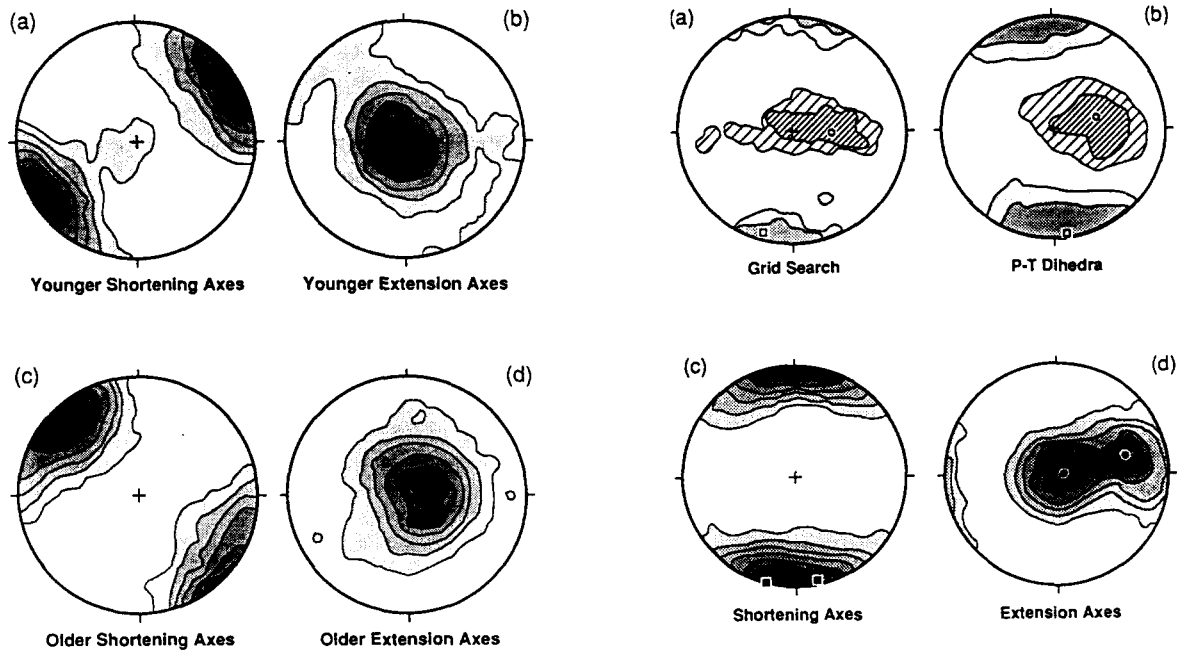Older Shortening Axes   Older Extension Axes

Fig. 12. Kinematically homogeneous subsets of fault-slip data from Quebrada del Toro. Data separated according to whether the kinematics of each fault measurement most closely resemble the younger or the older kinematic pattern. (a) & (b) Younger deformation ($N = 96$). (c) & (d) Older deformation ($N = 126$).

Forsyth 1984) and iterative numerical stress inversion (Julien & Cornet 1987). Integrating these results, we can understand the differences among the analytical results in terms of the geometry of the fault system. The results of the various analyses are shown in Table 3 and Fig. 13.

The results of grid search stress inversion (Fig. 13a and Table 3) (Gephart & Forsyth 1984) and the iterative numerical stress inversion (Table 3) (Julien & Cornet 1987) are virtually identical. The results of P–T dihedra stress inversion are similar to the results of the other stress inversions, both in terms of the directional distributions of good stress models (Fig. 13b) and the best model (Table 3). The moment tensor summation (Table 3) is dominated by the main shock, which was significantly different than many of the aftershocks. Because of this, the kinematic scale-invariance assumption of the graphical analysis is not rigorously met. Contours of the shortening and extension axes (Figs. 13c & d) are dominated by the numerous aftershocks and appear similar to the stress analysis methods. The graphical analysis does,
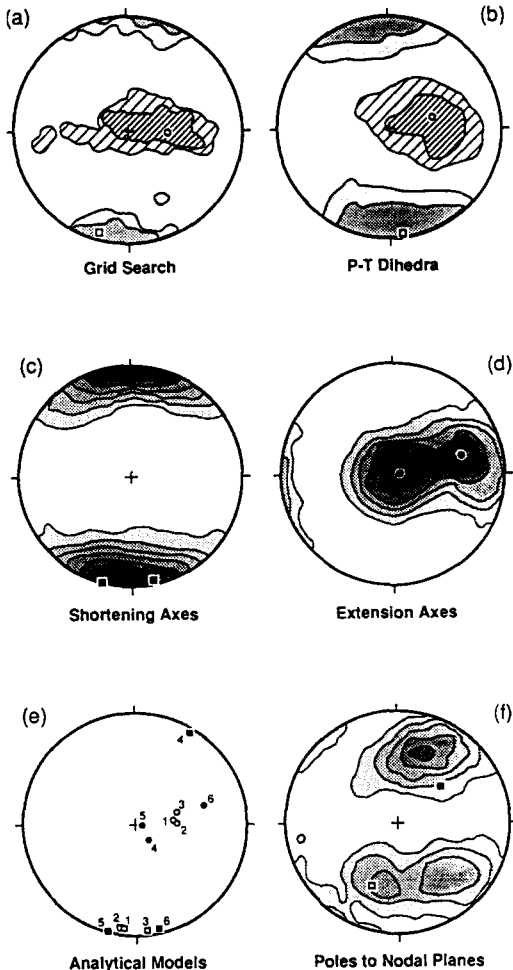

Grid Search   P-T Dihedra

Shortening Axes   Extension Axes

Analytical Models   Poles to Nodal Planes

Fig. 13. Analyses of fault-slip data from 1971 San Fernando, California, earthquake sequence ($N = 76$). Best models indicated with open boxes for σ_1, open dots for σ_3, solid boxes for shortening directions, and solid dots for extension directions. (a) Results of grid search stress inversion with 99% confidence area in light shading/ruling and 95% confidence area in dark shading/ruling (analysis provided by J. Gephart). (b) Results of P–T dihedra stress inversion with overlap of 56 dihedra in light shading/ruling and overlap of 66 dihedra in dark shading/ruling. (c) Shortening and (d) extension axes analyses of graphical kinematic method. (e) Comparison of best models. 1: grid search stress inversion (Gephart & Forsyth 1984); 2: iterative numerical stress inversion (Julien & Cornet 1987); 3: P–T dihedra stress inversion; 4: moment tensor summation; 5 and 6: graphical kinematic analysis. (f) Poles to faults and slip directions for 1971 San Fernando earthquake sequence data. Contour diagram of poles to nodal planes of fault-plane solutions ($N = 152$; each fault-plane solution has two nodal planes). Open box represents the pole to fault of the main event and the solid box represents the slip direction of the main event.

Table 3. Comparison of best models from analyses of fault-slip data from 1971 San Fernando earthquake sequence ($N = 76$). Results of grid search stress inversion and numerical iterative stress inversion from Gephart & Forsyth (1984) and Julien & Cornet (1987), respectively. Directions given in trend and plunge

Method of analysis	Maximum principal compression or shortening direction	Minimum principal compression or extension direction
Grid search stress inversion	187°, 07°	84°, 62°
Numerical iteration stress inversion	189°, 07°	89°, 59°
P–T dihedra stress inversion	173°, 05°	75°, 57°
Moment tensor summation	31°, 05°	139°, 75°
Graphical kinematic method	195°, 01°	94°, 85°
	168°, 05°	75°, 37°

Thrust Shortening   Thrust Extension
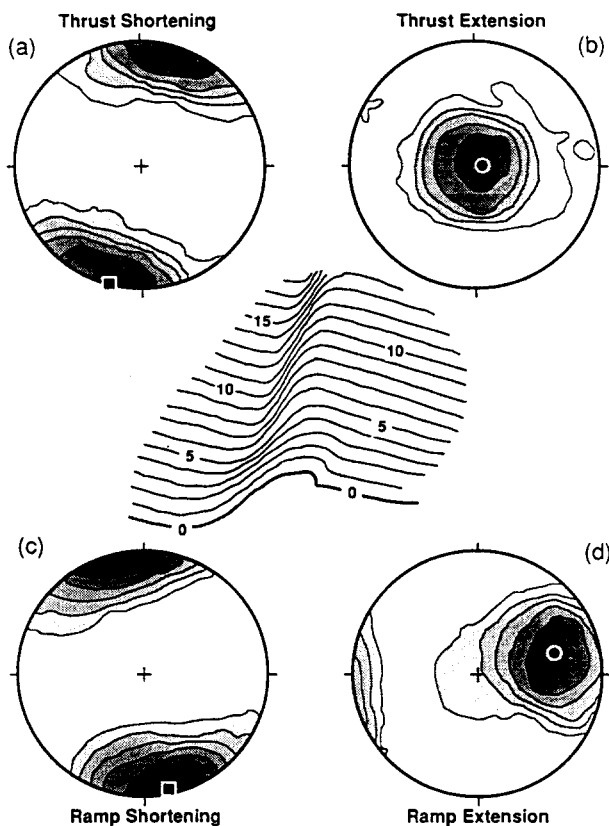

Ramp Shortening   Ramp Extension

Fig. 14. Kinematically homogeneous subsets of fault-slip data from 1971 San Fernando earthquake sequence. Data separated according to whether they have a pole to nodal plane closer to the moderately SSW-plunging maximum (N = 38) or the shallowly SE-plunging maximum (N = 38). (a) & (b) Kinematics of fault-plane solutions with SSW-plunging (thrust) nodal planes. (c) & (d) Kinematics of fault-plane solutions with SE-plunging (lateral ramp) nodal planes. Bingham distribution maxima of shortening and extension indicated with solid boxes and dots, respectively. In center is a schematic structural contour map showing simplified contours, in km, on the main fault plane (modified from Whitcomb et al. 1973). Dark 0 contour represents surface break.

however, display a bimodal distribution of extension axes, hinting at an explanation.

The differences between the results of the two kinematic analyses are a product of kinematic heterogeneity within the data set. Whitcomb et al. (1973) noted that two distinct kinds of fault plane solutions are common in the aftershock population: thrust events similar to the main shock and strike-slip events along a steeply NW-dipping fault or segment of the main fault. The extension axes of the two kinds of fault plane solutions are sufficiently different that they produce the distinct maxima (Fig. 13d) whereas the shortening axes are similar (Fig. 13c). Because the results of moment tensor summation are dominated by the main shock (thrust), they mostly reflect the kinematics of the thrust events.

Whitcomb et al. (1973) suggested that the presence of a large lateral ramp in the main fault (Fig. 14) caused the kinematic heterogeneity of the San Fernando earthquake sequence data, invoking the mechanism referred to here as strain compatibility (Fig. 9c). Aftershock locations and surface geologic data indicate that the main fault dips moderately to the NNE and that the lateral ramp dips steeply to the NW. Poles to the nodal

planes of the fault plane solutions show a moderately N-plunging point maximum and a distinct girdle with moderately SSW- and shallowly SE-plunging maxima (Fig. 13f). The SSW- and SE-plunging maxima indicate the orientations of the main fault and the lateral ramp, respectively, and the N-plunging maximum indicates their common slip direction. Two kinematically homogeneous subsets of the data can be obtained by separating the faults with SSW-plunging poles from faults with SE-plunging ones (Fig. 14 and Table 3).

The differences between dynamic and kinematic results (Fig. 13e and Table 3) might be interpreted in several ways: (1) the dynamic and/or kinematic methods may have failed; (2) their differences may be statistically insignificant; or (3) strain might have been non-coaxial with stress. The differences are not so great that one must consider the analyses failures. Indeed, there are considerable overlaps of acceptable models among the results of grid search inversion, P–T dihedra inversion and graphical kinematic analysis. Yet the consistency of the dynamic analyses, both internally and with results from adjacent areas in the Transverse Ranges and along the San Andreas Fault (Jones 1988), may suggest that the best models are more accurate than the statistics indicate. If so, the San Fernando earthquake sequence data represent strain which is non-coaxial with stress. The simplest explanation of the non-coaxiality is that the strain compatibility constraint, imposed by the lateral ramp in the main fault, prevents slip from occurring in the ideal direction.

The kinematics of subsets of the aftershock population defined by local magnitude (M) ranges show that both main fault and lateral ramp fault plane solutions are represented in all ranges of M < 5.0 (Fig. 15) but not above. The main shock is the only event with M >5.0 for which a fault plane solution was determined. The hypothesis of scale-invariant fault kinematics seems to break down at larger magnitudes, unless there was a large lateral ramp event for which a fault plane solution has not been determined. An unlocated coseismic event of M = 5.8 occurred 30 s after the main shock began (Hileman et al. 1975). This event may mark the beginning of activity on the lateral ramp of the main fault once the dislocation tip propagated to it. If this is the case, then the hypothesis of scale-invariant fault kinematics would be consistent with the data.

The various dynamic and kinematic methods of fault-slip analysis differ in terms of assumptions, computational intensity, and usefulness. While it may be argued that the assumptions of kinematic analysis are not obviously better than those of dynamic analysis, it may be that the former are more readily testable. The P–T dihedra stress inversion and the graphical kinematic method have the advantages that they are based on simple graphical constructions. As such they are more suitable for preliminary analysis in the field than the other methods, which are to varying degrees computationally intensive. Methods which produce results in graphical form (the grid search stress inversion, the P–T dihedra stress inversion and the graphical kinematic
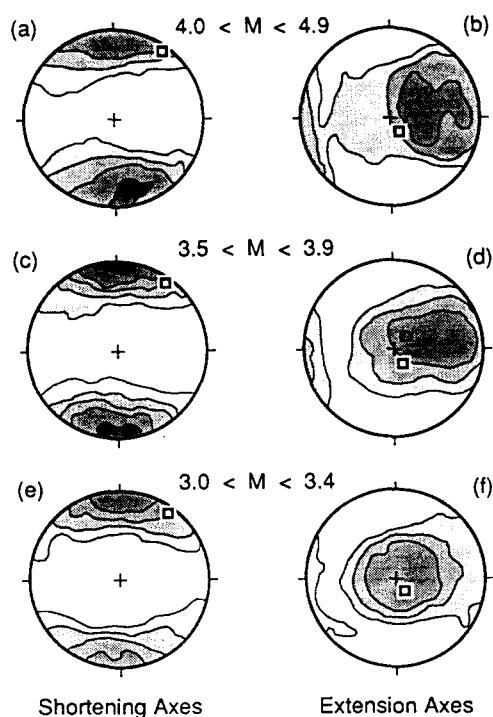
Shortening Axes   Extension Axes

Fig. 15. Fault-slip kinematics of data from 1971 San Fernando earthquake sequence representing different ranges of local magnitude (M). Open boxes represent kinematics of the main event (M = 6.4). (a) & (b) Kinematics of events with $4.0 \leq M \leq 4.9$ ($N = 17$). (c) & (d) Kinematics of events with $3.5 \leq M \leq 3.9$ ($N = 30$). (e) & (f) Kinematics of events with $3.0 \leq M \leq 3.4$ ($N = 28$).

method) are more useful than those which provide only a best model and no indication of the directional uncertainty. Graphical kinematic analysis may provide greater directional resolution than the other methods which did not discern the heterogeneity of the San Fernando earthquake sequence data.

CONCLUSIONS

Kinematic analysis of fault-slip data using the techniques outlined here provides quantitative and qualitative tools for understanding deformation in both modern and ancient orogens. The accuracy of constants relating fault gouge thickness and fault width with displacement may be improved by systematic collection of more data. But even without explicit evaluation of the constants, the scaling relationships are sufficient for the relative weighting of data and moment tensor summation. The graphical kinematic method is well suited for testing the assumptions of kinematic analysis. For the field data analyzed here, the assumptions seem to be reasonable. It might be that the assumptions generally hold for fault populations, which would give insight to the nature of the faulting process. For example, if fault-slip kinematics generally prove to be scale-invariant, then the fractal character of faulting is more profound than previously demonstrated. The graphical kinematic method is also useful for the analysis of kinematic heterogeneity. These techniques can be especially helpful in the field, where they may direct work toward key areas to resolve unforeseen problems.

A largely unexplored facet of fault-slip analysis is the potential to evaluate strain compatibility, material anisotropy, and material heterogeneity by integrating dynamic and kinematic results, such as done in a qualitative way here for the San Fernando earthquake sequence. This emphasizes that dynamic and kinematic analyses are complementary and that both types of analysis should be employed routinely in studies of fault-slip data.

REFERENCES

Aki, K. 1966. Generation and propagation of G waves from the Niigata earthquake of June 16, 1964, 2, Estimation of earthquake moment, released energy, and stress–strain drop from G wave spectrum. *Bull. Earthquake Res. Inst. Tokyo* **44**, 73–88.

Aleksandrowski, P. 1985. Graphical determination of principal stress directions for slickenside lineation populations: an attempt to modify Arthaud's method. *J. Struct. Geol.* **7**, 73–82.

Anderson, E. M. 1951. *The Dynamics of Faulting and Dyke Formation with Applications to Britain.* Oliver & Boyd, Edinburgh, U.K.

Angelier, J. 1984. Tectonic analysis of fault slip data sets. *J. geophys. Res.* **89**, 5835–5848.

Angelier, J. & Mechler, P. 1977. Sur une methode graphique de recherche des contraintes principales egalment utilisable en tectonique et en seismologie: la methode des diedres droits. *Bull. Soc. géol. Fr.* **19**, 1309–1318.

Armijo, R., Carey, E. & Cisternas, A. 1982. The inverse problem in microtectonics and the separation of tectonic phases. *Tectonophysics* **82**, 145–160.

Arthaud, F. 1969. Méthode de détermination graphique des directions de raccourcissement, d'allongement et intermédiare d'une population de failles. *Bull. Soc. géol. Fr.* **11**, 729–737.

Arthaud, F. & Mattauer, M. 1972. Sur l'origine tectonique de certains joints stylolitiques parallèles a la stratification; leur relation avec une phase de distension (exemple du Languedoc). *Bull. Soc. géol. Fr.* **14**, 12–17.

Aydin, A. & Reches, Z. 1982. Number and orientation of fault sets in the field and in experiments. *Geology* **10**, 107–112.

Barton, C. C., Samuel, J. K. & Page, W. R. 1988. Fractal scaling of fracture networks, trace lengths, and apertures (abs.). *Geol. Soc. Am. Abs. w. Prog.* **20**, A299.

Bott, M. H. P. 1959. The mechanisms of oblique slip faulting. *Geol. Mag.* **96**, 109–117.

Carey, E. & Brunier, B. 1974. Analyse théorique et numérique d'un modèle mécanique élémentaire appliqué à l'étude d'une population de failles. *C. r. Acad. Sci., Paris* **279D**, 891–894.

Chester, F. M. & Logan, J. M. 1987. Composite planar fabric of gouge from the Punchbowl Fault, California. *J. Stuct. Geol.* **9**, 621–634.

Cox, S. J. D. & Scholz, C. H. 1988. On the formation and growth of faults: an experimental study. *J. Struct. Geol.* **10**, 413–430.

Donath, F. A. 1962. Analysis of Basin-Range structure, south-central Oregon. *Bull. geol. Soc. Am.* **73**, 1–16.

Elliott, D. 1976. The energy balance and deformation mechanisms of thrust sheets. *Phil. Trans. R. Astr. Soc.* **A283**, 289–312.

Etchecopar, A., Vasseur, G. & Daignieres, M. 1981. An inverse problem in microtectonics for the determination of stress tensors from fault striation analysis. *J. Struct. Geol.* **3**, 51–65.

Gamond, J. F. 1987. Bridge structures as sense of displacement criteria in brittle fault zones. *J. Struct. Geol.* **9**, 609–620.

Gauthier, B. & Angelier, A. 1985. Fault tectonics and deformation: a method of quantification using field data. *Earth Planet Sci. Lett.* **74**, 137–148.

Gephart, J. W. 1988. On the use of stress inversion of fault-slip data to infer the frictional strength of rocks (abs.). *EOS Trans. Am. geophys. Un.* **69**, 1462.

Gephart, J. W. & Forsyth, D. W. 1984. An improved method for determining the regional stress tensor using earthquake focal mechanism data: application to the San Fernando earthquake sequence. *J. geophys. Res.* **89**, 9305–9320.

Hadley, D. & Kanamori, H. 1978. Recent seismicity in the San Fernando region and tectonics in the west-central Transverse Ranges, California. *Bull. seism. Soc. Am.* **68**, 1449–1457.

Higgs, W. G. & Williams, G. D. 1987. Displacement efficiency of faults and fractures. *J. Struct. Geol.* **9**, 371–374.

Hileman, J., Allen, C. & Nordquist, J. 1975. Seismicity of the Southern California region 1 January 1932 to 31 December 1972. Seismological Laboratory, California Institute of Technology, Pasadena, California.

Huang, Q. 1988. Computer-based method to separate heterogeneous sets of fault-slip data into sub-sets. *J. Struct. Geol.* **10**, 297–299.

Hull, J. 1988. Thickness-displacement relationships for deformation zones. *J. Struct. Geol.* **10**, 431–435.

Jackson, J. & McKenzie, D. 1988. The relationship between plate motions and seismic moment tensors, and the rates of active deformation in the Mediterranean and Middle East. *Geophys. J.* **93**, 45–73.

Jones, L. 1988. Focal mechanisms and the state of stress on the San Andreas fault in southern California. *J. geophys. Res.* **93**, 8869–8891.

Julien, Ph. & Cornet, F. 1987. Stress determination from aftershocks of the Campania-Lucania earthquake of November 23, 1980. *Annales Geophysicae* **5B**, 289–300.

Kamb, W. B. 1959. Ice petrofabric observations from Blue Glacier, Washington in relation to theory and experiment. *J. geophys. Res.* **64**, 1891–1909.

Kanamori, H. & Anderson, D. 1975. Theoretical basis of some empirical relations in seismology. *Bull. seism. Soc. Am.* **65**, 1075–1095.

King, G. C. P. 1983. The accommodation of large strains in the upper lithosphere of the Earth and other solids by self-similar fault systems: the geometrical origin of b-value. *Pure & Appl. Geophys.* **121**, 761–815.

Kostrov, B. V. 1974. Seismic moment and energy of earthquakes, and seismic flow of rock. *Izv. Acad. Sci. USSR Phys. Solid Earth* **1**, 23–44.

Krantz, R. W. 1988. Multiple fault sets and three-dimensional strain: theory and application. *J. Struct. Geol.* **10**, 225–237.

Langston, C. A. 1978. The February 9, 1971 San Fernando earthquake: a study of source finiteness in teleseismic body waves. *Bull. seism. Soc. Am.* **68**, 1–29.

Lisle, R. J. 1987. Principal stress orientations from faults: an additional constraint. *Annales Tectonicae* **1**, 155–158.

Mardia, K. V. 1972. *Statistics of Directional Data*. Academic Press, London, U.K.

Marrett, R. 1990. The late Cenozoic tectonic evolution of the Puna plateau and adjacent foreland, northwestern Argentine Andes. Unpublished Ph.D. dissertation, Cornell University, Ithaca, New York.

Marrett, R., Allmendinger, R. W. & Grier, M. E. 1989. Kinematic changes during late Cenozoic deformation of the southern Puna plateau: Argentine Andes, 23°S–27°S Latitude. *Proc. 28th Int. Geol. Congr.* **2**, 372–373.

Means, W. D. 1987. A newly recognized type of slickenside striation. *J. Struct. Geol.* **9**, 585–590.

Michael, A. J. 1984. Determination of stress from slip data: faults and folds. *J. geophys. Res.* **89**, 11,517–11,526.

Molnar, P. 1983. Average regional strain due to slip on numerous faults of different orientations. *J. geophys. Res.* **88**, 6430–6432.

Muraoka, H. & Kamata, H. 1983. Displacement distribution along minor fault traces. *J. Struct. Geol.* **5**, 483–495.

Omarini, R. H. 1983. Caracterización litológica, diferenciación y génesis de la Formación Puncoviscana entre el Valle de Lerma y la Faja Eruptiva de la Puna. Unpublished Ph.D. dissertation Universidad Nacional de Salta, Salta, Argentina.

Petit, J.-P. 1987. Criteria for the sense of movement on fault surfaces in brittle rocks. *J. Struct. Geol.* **9**, 597–608.

Power, W. L., Tullis, T. E., Brown, S. R., Boitnott, G. N. & Scholz, C. H. 1987. Roughness of natural fault surfaces. *Geophys. Res. Lett.* **14**, 29–32.

Power, W. L., Tullis, T. E. & Weeks, J. D. 1988. Roughness and wear during brittle faulting. *J. geophys. Res.* **93**, 15,268–15,278.

Reches, Z. 1983. Faulting of rocks in three-dimensional strain fields—II. Theoretical analysis. *Tectonophysics* **95**, 133–156.

Reches, Z. 1987. Determination of the tectonic stress tensor from slip along faults that obey the Coulomb yield condition. *Tectonics* **6**, 849–861.

Reches, Z. & Dieterich, J. 1983. Faulting of rocks in three-dimensional strain fields: I. Failure of rocks in polyaxial, servo-control experiments. *Tectonophysics* **95**, 111–132.

Sammis, C., King, G. C. P. & Biegel, R. 1987. Kinematics of gouge formation. *Pure & Appl. Geophys.* **125**, 777–812.

Scholz, C. H. 1987. Wear and gouge formation in brittle faulting. *Geology* **15**, 493–495.

Scholz, C. H. & Aviles, C. A. 1986. The fractal geometry of faults and faulting. In: *Earthquakes Source Mechanics* (edited by Das, S., Boatwright, J. & Scholz, C.). Am. Geophys. Un. Geophys. Monogr. **37**, 147–156.

Turcotte, D. L. 1986. A fractal model for crustal deformation. *Tectonophysics* **132**, 261–269.

Wallace, R. E. 1951. Geometry of shearing stress and relation to faulting. *J. Geol.* **59**, 118–130.

Walsh, J. J. & Watterson, J. 1987. Distributions of cumulative displacement and seismic slip on a single normal fault surface. *J. Struct. Geol.* **9**, 1039–1046.

Walsh, J. J. & Watterson, J. 1988. Analysis of the relationship between displacements and dimensions of faults. *J. Struct. Geol.* **10**, 239–247.

Whitcomb, J. H., Allen, C. R., Garmany, J. D. & Hileman, J. A. 1973. San Fernando earthquake series, 1971: focal mechanisms and tectonics. *Rev. Geophys. & Space Phys.* **11**, 693–730.

Wojtal, S. 1989. Measuring displacement gradients and strains in faulted rocks. *J. Struct. Geol.* **11**, 669–678.